Validation of a Digital Noise Power Integration Technique for Radiometric Clear Sky Attenuation Estimation at Q-Band

Alexios Costouri[ID], James Nessel[ID], *Member, IEEE*, and George Goussetis[ID], *Senior Member, IEEE*

Abstract— This article presents the validation of a digital signal processing technique that can be used to estimate radiometric sky noise, and hence atmospheric absorption, within existing digital receivers at little/no additional cost. To demonstrate this, a receiver was constructed that simultaneously records the beacon signal power from the ALPHASAT Aldo Paraboni technology demonstration payload, as well as the integrated noise power in the adjacent band. Calibration from the digital radiometer is performed using tip-curve calibration procedures. Atmospheric fading is then obtained by observing the beacon as well as the radiometric signals. This enables the comparison of fading obtained by the two techniques and provides a means to calibrate the received beacon power level to obtain total atmospheric attenuation. It is shown that for low levels of fading, up to a few dB, the two techniques provide good agreement. This approach can, therefore, provide a low-cost option for geostationary mm-wave satellite channel measurements in the low fading regime, which can be useful in the design and operation of the feeder links in emerging satcom systems.

Index Terms— ALPHASAT, calibration, propagation, *Q*-band, radiometer, software-defined radio (SDR), tip curve.

I. INTRODUCTION

THE trends toward broadband services, high-throughput satellites, and reduction of the per MB/s cost drive the use of ever higher frequencies in satellite communications. While the use of Ka-band is now well established, there is an increasing interest in higher bands, such as Q-/V-bands (40/50 GHz) [1] and W-band [2]. Broad bandwidths available at these frequency bands offer attractive opportunities for exploitation in the feeder links since they can support high capacity with fewer gateways. Consequently, the cost of the ground segment is reduced, while the entire Ka-band

becomes available for revenue-raising user links [3]. The aforementioned developments motivate the characterization of atmospheric propagation effects and their properties at mm-wave frequencies. An early campaign to experimentally characterize atmospheric propagation effects beyond the Ka-band was made with the ITALSAT F1 satellite which carried beacons covering Europe at three bands, Ka-, Q-, and V-bands (20, 40, and 50 GHz, respectively) [4], [5]. Presently, the Aldo Paraboni payload hosted onboard the ALPHASAT satellite delivers beacons with similar coverage at Ka- and Q-bands (19.701 and 39.402 GHz) underpinning an ongoing Europe-wide test campaign [6], [7]. Anticipating future needs for characterization at W-band, ESA is currently making preparations for a beacon at these frequencies in geostationary orbit [2].

While beacons onboard geostationary satellites provide a very accurate methodology to characterize the channel from this orbit, such missions are costly and typically require long developments prior to launching. To this end, alternative methodologies are currently explored, such as the characterization of W-band propagation using cubesats [8] or from purely ground-based observations [9]. In particular, passive cosmic background radiometry represents a popular methodology to characterize atmospheric fading [10]. This technique is based on measuring received noise from a portion of the sky without radio emitters. By virtue of calibrating the received noise, which is a combination of atmospheric emission and cosmic background radiation, atmospheric fading can be estimated without relying on a spaceborne beacon. This methodology delivers its maximum accuracy when the effects of larger atmospheric particles can be neglected, e.g., in the absence of precipitation.

The primary aim of this article is to experimentally evaluate the potential of a software-defined radio (SDR) receiver to deliver aforementioned passive radiometry measurements and characterize the geostationary channel at the satellite downlink without disrupting nominal operations. This is achieved as a result of measurements performed with a bespoke terminal designed to receive the Q-band signal from the beacon of the ALPHASAT Aldo Paraboni payload [11]. By virtue of the SDR setup, where a downconverted image of the received signal is sampled and digitally processed to obtain its spectrum, it is possible to simultaneously record the level of the intended signal (in this case, a CW beacon), as well as the

noise in the nearby frequency band. The specific configuration enables an accurate comparison of the atmospheric attenuation derived from the radiometer, with that obtained from the beacon observation. Earlier literature, such as [12] and [13], concurrently recorded the beacon satellite signal and noise power at Ka- and Q-bands in which the calibration of the radiometer in postprocessing required the satellite beacon measurements. Furthermore, in [14] and [15], the concurrent recordings helped to monitor events and obtain reference levels to estimate attenuation templates. The proposed configuration provides a potential method for operational ground stations to monitor fading in real time with no additional hardware required.

The remainder of this article is organized as follows. Section II outlines the theory underpinning the radiometric measurement and calibration. Section III presents some details of the system and the performed calibrations. Section IV presents the comparative experimental results between the fading obtained from the beacon and the radiometric measurements. Finally, conclusions are presented in Section V.

II. PRINCIPLE OF OPERATION

An electromagnetic signal that propagates through the atmosphere experiences attenuation due to absorption and scattering. Excluding free-space losses (FSLs), the signal attenuation along a path (also referred to as the extinction of the signal) can be obtained as [10]

$$A_t = A_{ab} + A_{sc} \text{ (dB)} \tag{1}$$

where A_t is the total attenuation along the signal path, A_{ab} is the attenuation due to absorption, and A_{sc} is the attenuation due to scattering.

The attenuation due to absorption is attributed to the interaction of electromagnetic energy with the gaseous molecules (primarily oxygen and water vapor in the 1–100 GHz range). At thermal equilibrium, energy transitions of these particles lead to emission and absorption of electromagnetic energy at equal rates. With this assumption, a signal propagating along a given path in the atmosphere will, therefore, experience atmospheric (or gaseous) absorption at the same rate [10]. Gaseous absorption dominates fading when, in the radiative transfer equation, the effects of scattering or other absorptive mechanisms of electromagnetic wave from atmospheric particles can be neglected [10]. This typically applies in, e.g., the absence of precipitation. In this case, gaseous absorption can be characterized by measuring the received noise power by considering the thermodynamics of the atmosphere as briefly outlined next.

Commencing from the radiative transfer equation and assuming that the atmosphere can be considered in thermal equilibrium, it can be shown that the atmospheric absorption can be approximated as [10]

$$A_{ab} = 10 \, log_{10} \frac{T_m - T_c}{T_m - T_B} \text{ (dB)}. \tag{2}$$

In (2) T_B, T_m, and T_c correspond to the brightness, mean brightness, and cosmic radiation temperatures, respectively.

The brightness temperature T_B represents the temperature of a blackbody in thermal equilibrium that would have the same brightness at the frequency of interest as the isotropic atmosphere [10]. The term T_m stands for the mean radiating temperature of the atmosphere/absorbing medium [10]. Available guidelines (ITU-R P.618-13 [16]) provide empirical expressions to obtain T_m as a function of the surface temperature T_s for clear and cloudy weather, as in the following equation:

$$T_m = 37.34 + 0.81 T_s \text{ (K)}. \tag{3}$$

The cosmic radiation temperature T_c accounts for the contribution from the cosmic radiation associated with the remnants from the Big Bang at the mm-/micro-wave range and has a constant value of 2.7 K [17].

The above suggests that the gaseous absorption of the atmosphere can be estimated once the values of the atmosphere's brightness temperature T_B are available. The latter can be obtained by exploiting radiometric noise measurements. In particular, a lossless antenna enclosed in a blackbody in thermal equilibrium (which with the abovementioned approximation can be assumed to be the atmosphere) will detect the following noise power [17]:

$$P_{N*} = kT_B B \text{ (W)} \tag{4}$$

where P_{N*} is the noise power received by the antenna over a certain bandwidth B, with k being Boltzmann's constant and T_B the brightness temperature in kelvin. Consequently, the noise temperature of a clear sky is proportional to the noise power recorded in an ideal receiver comprising a lossless antenna and noise-free electronics.

For practical receivers, additional considerations are required. The RF electronics generate noise that can be calculated from the noise figure of each component, which can then be converted to an equivalent noise temperature, T_r [18]. Furthermore, a practical antenna is not lossless but instead is characterized by a noise temperature T_N. Moreover, in addition to the main lobe (which observes the desired brightness temperature T_B), the antenna also has sidelobes that capture noise from unwanted sources and the contributions are represented by T_{sl}. The total gain G of the receiver system must also be considered since gain applies to both the noise and desired signal. With the abovementioned considerations, (4) for a lossy receiver system becomes [17]

$$P_N = (T_B + T_{sl} + T_r + T_N)kBG \text{ (W)}. \tag{5}$$

Rearranging the equation to brightness temperature

$$T_B = \frac{P_N}{kBG} - (T_{sl} + T_r + T_N) \text{ (K)}. \tag{6}$$

Recognizing the dependence of the brightness temperature T_B on the measured noise power P_N, (6) can be written in the format

$$T_B = a P_N + b \text{ (K)} \tag{7}$$

where the coefficients a and b stand for

$$a = \frac{1}{kBG} \text{ (K J}^{-1}\text{Hz}^{-1}) \tag{8}$$

$$b = -(T_{sl} + T_r + T_N) \text{ (K)}. \tag{9}$$

While approximate estimations for the coefficients a and b can be obtained by (8) and (9), more accurate values can be obtained by performing experimental calibration to remove the system's gain, noise, and antenna sidelobe contributions from the recorded noise power. A tip calibration exploits the fact that directions closer to the horizon experience longer paths through the atmosphere and consequently are associated with higher attenuation (and thus atmospheric noise) levels [19]. On the assumption that the atmosphere is homogeneous with constant density, the attenuation A_{ab} at a given elevation angle θ is proportional to the optical path length at that angle normalized to that at zenith. This term is also known as air mass and for elevation angles over $10°$, where the Earth's curvature can to a good approximation be neglected, is obtained from simple trigonometry [10], [20]

$$Air\ mass = \frac{1}{sin(\theta)} = csc(\theta). \qquad (10)$$

On that basis, the attenuation A_{ab} at angle θ is linked with the attenuation A_{ab90} at zenith ($\theta = 90°$) according to

$$A_{ab} = A_{ab90}csc(\theta) = A_{ab90} * Air\ mass\ \text{(dB)}. \qquad (11)$$

Equation (11) reveals that the relationship between air mass and attenuation is linear and the associated curve (also referred to as tip curve) crosses the origin. It is noted that although an air mass lower than unity is practically impossible, theoretically, this extrapolation is meaningful. In particular, air mass of zero corresponds to the absence of the atmosphere and, therefore, no attenuation of a signal [17].

During tip calibration, the antenna is pointed at different elevation angles, corresponding to different values for the air mass, and the noise power is recorded. An initial estimation of the zenith attenuation, A_{ab90} in dB, can be calculated by comparing two elevation angles [19]

$$A_{ab90} = \frac{4.343}{csc(\theta) - 1}\ ln\frac{T_{B90} - T_m}{T_B(\theta) - T_m}\ \text{(dB)} \qquad (12)$$

where T_{B90} and $T_B(\theta)$ are the brightness temperature at zenith and at an elevation angle θ, respectively. The temperatures T_{B90}, $T_B(\theta)$, and T_m in (12) are unknown. Given that, as per (7), the relationship between measured noise power and temperature is linear, (12) can be rewritten in terms of the associated integrated noise power levels

$$A_{ab90} = \frac{4.343}{csc(\theta) - 1}ln\frac{P_N(T_{B90}) - P_N(T_m)}{P_N(T_B(\theta)) - P_N(T_m)}\ \text{(dB)}. \qquad (13)$$

To a first approximation, the mean radiating temperature T_m can be replaced with that of the ambient air temperature T_a. In turn, the integrated noise power associated with the ambient temperature $P_N(T_a)$ can be replaced with the observation of the brightness of a blackbody at ambient temperature. Therefore, (13) can be rewritten as

$$A_{ab90} = \frac{4.343}{csc(\theta) - 1}ln\frac{P_N(T_{B90}) - P_N(T_a)}{P_N(T_B(\theta)) - P_N(T_a)}\ \text{(dB)} \qquad (14)$$

and a first estimate of the calibration coefficients can be made as

$$a_{est} = \frac{e^{A_{ab90}/4.343}(T_c - T_a)}{P_N(T_{B90}) - P_N(T_a)}\ \text{(K J}^{-1}\text{ Hz}^{-1}) \qquad (15)$$

$$b_{est} = T_a - a_{est}(P_N(T_a))\ \text{(K)}. \qquad (16)$$

Fig. 1. Photograph of the receiver.

Next, we consider that the mean brightness temperature differs from the blackbody observed at ambient temperature

$$\Delta T = T_a - T_m\ \text{(K)}. \qquad (17)$$

Consequently, the initial estimation of a_{est} can be used to find more accurate values of $P_N(T_m)$ as

$$P_N(T_m) = P_N(T_a) - \frac{\Delta T}{a_{est}}\ \text{(W)}. \qquad (18)$$

The updated calibration coefficients, a_{est*} and b_{est*}, and updated at zenith, A_{ab90*}, can then be obtained by introducing (18) into (14)–(16)

$$A_{ab90*} = \frac{4.343}{csc(\theta) - 1}ln\frac{P_N(T_{B90}) - P_N(T_m)}{P_N(T_B(\theta)) - P_N(T_m)}\ \text{(dB)} \qquad (19)$$

$$a_{est*} = \frac{e^{A_{ab90*}/4.343}(T_c - T_a - \Delta T)}{P_N(T_{B90}) - P_N(T_m)}\ \text{(K J}^{-1}\text{ Hz}^{-1}) \qquad (20)$$

$$b_{est*} = T_a - \Delta T - a_{est*}(P_N(T_a))\ \text{(K)}. \qquad (21)$$

In a tip calibration process, the calibration coefficients are estimated for the original approximation $T_m = T_a$. Based on this estimation, the tip curve (i.e., attenuation versus airmass) is then plotted. Typically, the original tip curve does not cross the origin due to the nonzero value of ΔT in (17). To this end, an initial assumption of ΔT is made and the updated calibration coefficients, a_{est*} and b_{est*} are calculated. Rapid convergence of the calibration coefficients is achieved by iterating (18)–(21) with the assumed ΔT. The latest calculated calibration coefficients are used in each iteration. The correct calibration coefficients are calculated by adjusting ΔT until the tip-curve plot extrapolates to zero.
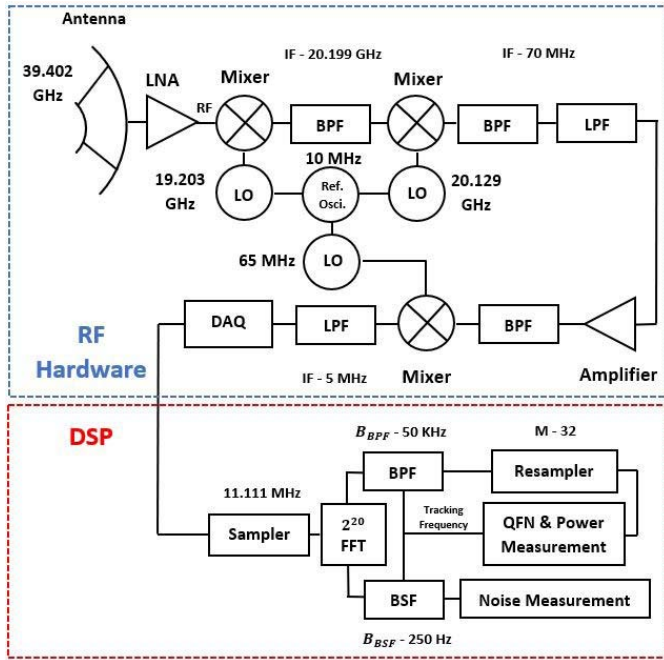
Fig. 2.   Beacon receiver RF hardware (top) and DSP (bottom) block diagram.

Fig. 3.   Decimated IF spectrum with beacon signal present.

III. SDR RECEIVER

The opportunities and limitations to characterize fading using the aforementioned radiometric approach at the Q-band satellite downlink frequency using a low-cost SDR receiver are next investigated by means of an experimental setup. The latter involves a Q-band receiver mounted on a pointing system shown in Fig. 1 that tracks the ALPHASAT satellite using an open-loop system based on ephemeris data. The remainder of this section provides a description of the SDR receiver and its calibration.

A. System Description

The RF and digital signal processing (DSP) block diagram of the SDR Receiver is shown in Fig. 2. The receiver captures a linearly polarized signal at Q-band which is downconverted to an intermediate frequency (IF) of 5 MHz exploiting three-stage mixing. An ultrastable 10-MHz reference oscillator is used across the three downconversion stages. The hardware is in a thermally insulated housing whose internal temperature is recorded. The signal is digitized at the 5 MHz IF frequency using a 12 bit National Instruments 5124 data acquisition (DAQ) card, which samples at a rate of 11.111 MHz.

The time-domain sampled signal is converted to the frequency domain exploiting a fast Fourier transform (FFT) on 2^{20} time-domain samples, leading to a resolution of 10.6 Hz. Then, a digital 50 kHz, tenth-order type 2 Chebyshev bandpass filter (BPF) is applied to isolate the beacon signal and the resulting spectrum is digitally resampled by a factor of 32 to reduce processing time, as shown in Fig. 2. A novel digital routine enables tracking any frequency drift of the beacon signal and together its peak power level [21]. Moreover, the Quinn–Fernandes–Nessel (QFN) routine centers the filter
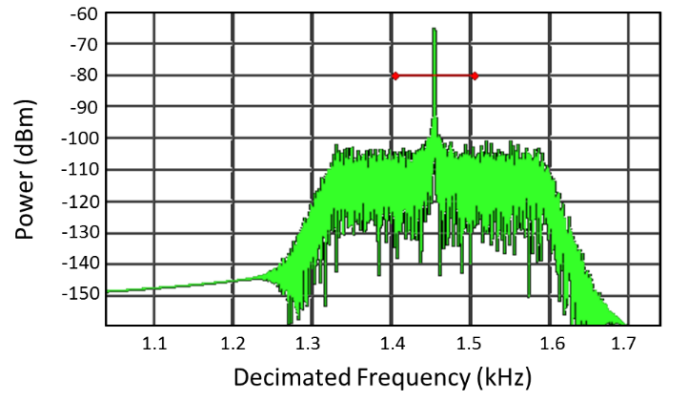
accordingly. This routine is a variant of the Quinn–Fernandes frequency estimator [22], which uses *a priori* information window on the frequency that the beacon is expected to appear, resulting in faster detection. This allows minimizing scalloping losses as the QFN estimator interpolates the FFT and the total power of the beacon is recorded.

A typical image of the decimated spectrum detected by the SDR receiver is shown in Fig. 3. The received beacon power is recorded at 10 and 1 Hz. These are then used in conjunction with atmospheric data provided by the European Centre for Medium-Range Weather Forecasts (ECMWF) vertical profiles and weather station data to produce a reference level such that the gaseous absorption and excess attenuation can be estimated [13]. The ECMWF data are available for every 6 h on a regular latitude/longitude grid with $0.125° \times 0.125°$ spatial resolution. The ECMWF vertical profile data (temperature, humidity, and pressure) are processed with the well-known mass absorption models by Liebe *et al.* [23] and Rosenkranz [24] and the total path attenuation composed of oxygen, water vapor, and cloud path attenuation is thereby obtained for the site. Identification of nonrainy periods is made from the weather station data, and in conjunction with the ECMWF data, a daily averaged gaseous attenuation level can be estimated. Once the reference attenuation level has been calculated for each day, it is subtracted from the measured power time series to produce the total atmospheric attenuation (including gaseous losses). Example of calibrated time series with the abovementioned approach can be seen in [11], [25], and [26]. A more detailed description of the receiver can be found in [13].

A digital tenth-order Type 2 Chebyshev bandstop filter (BSF) with a rejection bandwidth B_{BSF} of 250 Hz is concurrently applied on the spectrum resulting from the FFT, as shown in Fig. 2. The center of the digital BSF is defined by the QFN frequency estimation of the beacon signal. This operation enables to virtually suppress the beacon signal from the received spectrum and hence allowing the integration of the noise power measurement over the full IF bandwidth of 1 MHz. A type 2 Chebychev filter, unlike a type 1, has a flat bandpass response. An instance of the BSF response is plotted in Fig. 4. It is noted that the Aldo Paraboni beacon signal is a continuous wave signal (not modulated) with low phase
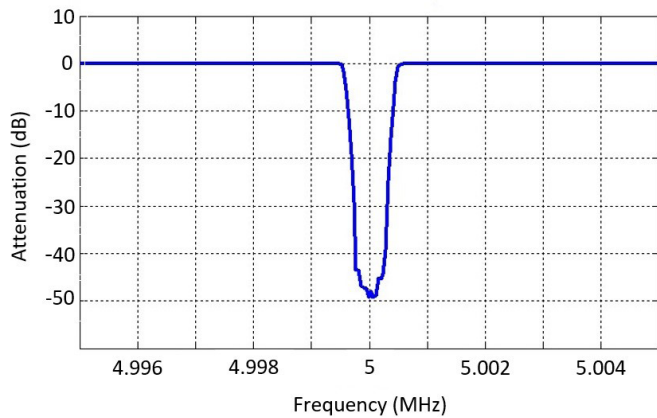
Fig. 4. Digital notch filter response for measuring the noise power of the beacon.
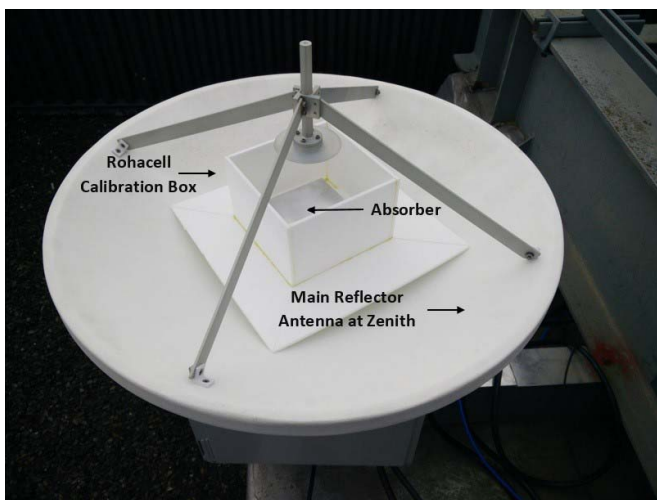

Fig. 5. Reflector at zenith to accommodate the calibration box during the hot-cold experiment.
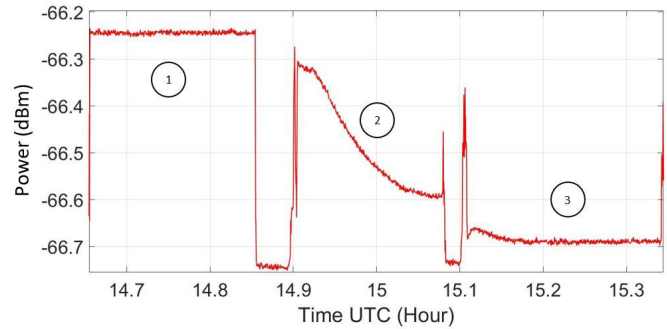

Fig. 6. Noise power recorded during the hot-cold target experiment. Different phases are marked as: 1) noise power with absorber at air temperature; 2) noise power with absorber immersed in liquid nitrogen (failed attempt); and 3) noise power with absorber immersed in liquid nitrogen (successful attempt).

noise (theoretically no bandwidth) and, hence, the choice of the narrow bandwidth notch filter. The integrated noise power is logged with the same frequency as the beacon signal.

The capability of this receiver to perform as a low-cost radiometer is next demonstrated by means of a hot-cold target experiment. A radar absorbing material (RAM) with sharp 5 mm tall pyramidal and total tile dimensions of 100×100 mm injection molded conductive plastic, with reflection below 45 dB at 40 GHz, was used as a blackbody target [27]. A cuboid box was built to host the RAM absorber using Rohacell (relative dielectric permittivity $\varepsilon r = 1.05$) and hence largely RF transparent. The box was of sufficient dimensions to be accommodated on the dish, while the RAM absorber fully covered the antenna feed. Throughout the experiment, the antenna was pointed to zenith for easy access as well as providing a level plane for the calibration box to rest upon (see Fig. 5). During the experiment, the integrated noise power was measured for two different temperatures of the blackbody target, in particular the ambient air during the procedure (hot temperature measured at 280 K) and liquid nitrogen (cold temperature approximately at 77 K). The ambient air temperature during the calibration was recorded from a nearby weather station (building south of the receiver at a distance of approximately 70 m) at 1 min intervals.

In order for the absorber to first acquire the ambient (hot) temperature, it was left outdoors under shade for an hour. The absorber was then placed at the bottom of the box and the first measurement was recorded. In order to then obtain the cold source measurement, liquid nitrogen was introduced in the host Rohacell box. During the first attempt, it was not possible for the absorber to acquire the cold temperature as it started floating in the liquid nitrogen. A second attempt was made with the addition of an aluminum block on top of the absorber in order to add weight. The second attempt was successful and this can be seen in Fig. 6 where the integrated noise power time series during the calibration process is shown. Liquid nitrogen was added twice, as the first time the liquid boiled and evaporated within minutes due to the addition of the aluminum block. The results in Fig. 6 indicate that an approximate blackbody target transitioning from 280 to 77 K results in a differential integrated noise power level of 0.45 dB. Fig. 7, plots the hot and cold target temperature (in Kelvin), against the recorded integrated noise power.

B. Calibration

The tip-curve calibration described in Section II was performed during a clear sky day. The receiver antenna elevation angle was tipped at the elevation angles of 15°, 20°, 30°, 45°, 60°, and 90° and the channel noise was recorded. The ambient temperature target measurements recorded in the hot-cold experiment were used in the first approximation of the coefficients and attenuation. Fig. 8 shows the results of the initial and corrected calibration coefficients. ΔT was adjusted to satisfy the assumption of no attenuation at an air mass of zero, the corrected coefficients are obtained as

$$a = 8.98 * 10^{12} \text{ K J}^{-1} \text{ Hz}^{-1}, \quad b = -1841 \text{ K}.$$

Furthermore, receiver gain variations due to temperature can impact the accuracy of the radiometer and can be compensated by performing a temperature calibration. To combat gain variation, in the work of [28] and [29], a reference noise source was added between the antenna and the low noise block via a coupler. Due to hardware limitations, such calibration
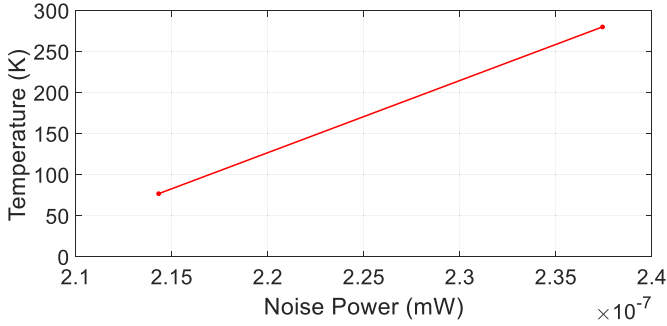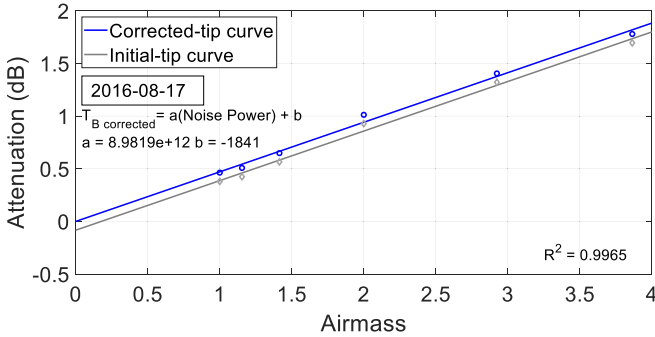
Fig. 7.   Hot–cold experiment plot.

Fig. 8.   Tip-curve calibration. Blue line: corrected tip. Gray line: initial tip. Coefficient of determination (R^2) is 0.9964.

TABLE I
RADIOMETER ATMOSPHERIC ABSORPTION IN CLEAR SKY THROUGHOUT CLEAR SKY SEGMENT

Hour	Temp (°C)	T_B (K)	T_m (K)	A_{ab} (dB)	Beacon (dBm)
1	10.90	72.49	267.42	1.33	-64.65
2	10.00	71.99	266.69	1.32	-64.61
3	9.42	71.76	266.22	1.32	-64.60
4	8.74	72.14	265.67	1.33	-64.61
5	8.55	68.11	265.51	1.24	-64.57
6	8.62	66.86	265.57	1.22	-64.52
7	9.75	62.89	266.50	1.12	-64.46
8	10.91	59.69	267.43	1.05	-64.38
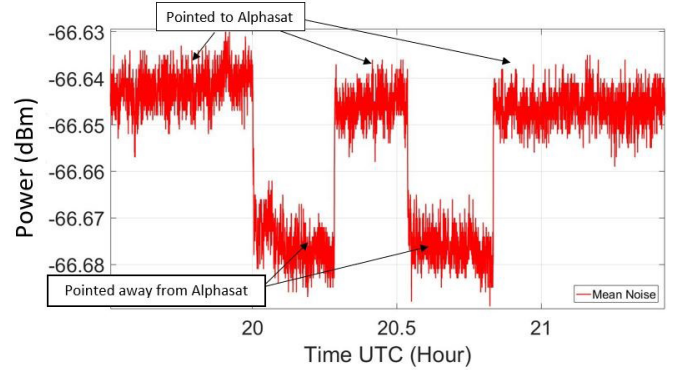
Fig. 9.   Noise power recorded when pointed toward and away from ALPHASAT Aldo Paraboni beacon.

has not been performed. Nonetheless, to mitigate such errors, as mentioned in Section III, the receiver is thermally insulated. Furthermore, the temperature variation of the low noise amplifier was observed to be stable with ±2 °C variations from the mean temperature.

The corrected coefficients obtained from the tip-curve calibration have been used to obtain the brightness temperature in the rest of this article.

IV. EXPERIMENTAL RESULTS

The calibration performed in Section III is next applied to the measurement of atmospheric fading at Q-band. In order to enable concurrent measurements from the beacon and radiometric signals, the receiver was pointed to the geostationary ALPHASAT satellite.

In order to confirm the efficacy of the digital filtering in suppressing beacon signal power from being injected into the integrated noise, an experiment is conducted. In particular, measurements of the integrated noise are recorded when pointing the receiver at two different positions: while pointing to the ALPHASAT satellite and while pointing at a small angle away from the satellite during clear sky. The results are plotted in Fig. 9, where the measurements taken at the two positions of the receiver are marked. As shown, there is a small level of additional noise (approximately 0.03 dB) recorded when the receiver points to the beacon. This increase is attributed to leakage of the beacon signal into the integrated noise.

In order to remove this contribution, the additional noise source was modeled as a temperature increase [13] as the sun's

radiation in [30] was modeled as a contribution to brightness temperature. Furthermore, considering that the temperature and power are linearly related

$$P_N(alpha) = P_N(away) + P_N(sat)e^{-(Att/4.343)} \qquad (22)$$

where $P_N(alpha)$ is the noise power measurement when tracking the satellite beacon, $P_N(away)$ is the noise power measurement when pointing away from the satellite beacon, $P_N(sat)$ is the satellite signal noise contribution in the absence of atmospheric attenuation, and Att is the path attenuation. The path attenuation Att during the measurement period was obtained from the ECMWF data. Once this bias is obtained, $P_N(sat)$ is subtracted from the noise power measurements.

With noise bias from the beacon removed, estimations of the brightness temperature of the sky can be calculated from the integrated noise with the described method in Section II. To check for any gain variations caused by temperature fluctuations, the estimated brightness temperature and received beacon power were plotted during a clear sky segment (see Fig. 10). Mild temperature fluctuations during clear sky are expected to have minor changes on the estimated brightness temperature and received beacon power assuming no gain variations. The estimated brightness temperatures T_B mean brightness temperature T_m, atmospheric absorption A_{ab}, and beacon signal at the different hours are reported in Table I. Reported temperatures in Fig. 10 (orange) and Table I from the nearby weather station were used to calculate T_m using (3) and A_{ab} was calculated using (2). A fluctuation of T_B and therefore A_{ab} can be seen in the period between hour 4 and 8 in which the temperature increased 2.4 °C. The difference
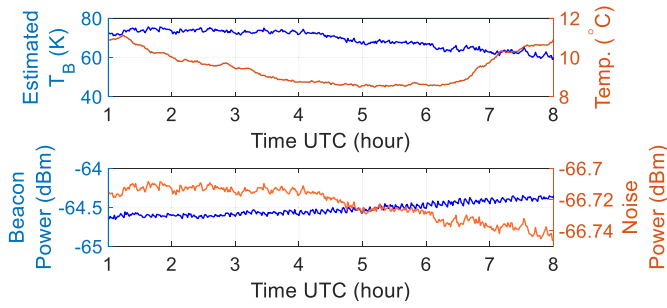
Fig. 10. Estimated brightness temperature (blue) with temperature (orange) superimposed (top) and received beacon power (blue) with integrated noise power (orange) superimposed (bottom) during a clear sky segment.
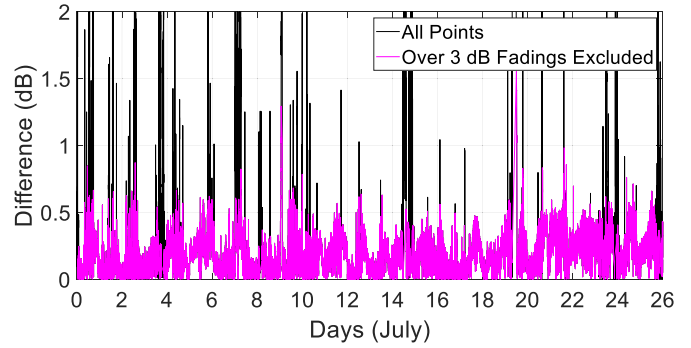

Fig. 12. Beacon derived and noise derived attenuation difference with all points included (black) and with over 3 dB fadings excluded (magenta).
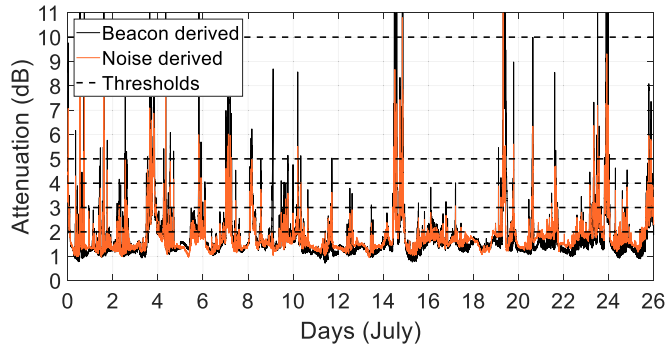

Fig. 11. Atmospheric attenuation for July 2016. Black: atmospheric attenuation derived through power measurements. Orange: atmospheric attenuation derived through the noise power measurements. Black dashed line: different thresholds.
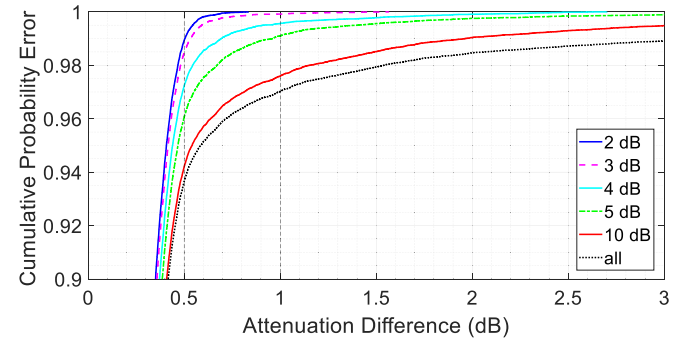

Fig. 13. CDF of the attenuation difference between the beacon derived and noise derived attenuation for July 2016 including all points (black dotted line) and the shown thresholds.

in atmospheric absorption between hours 1 and 5 is 0.09 dB, which can also be seen at the beacon signal as well. This indicates that the radiometer is operating as expected with no noticeable gain variations since integrated noise power and brightness temperature decreases with an increase in received beacon power.

The noise derived attenuation shown in Fig. 11 (in orange) for a period of 26 days in July 2016 is obtained by the method described previously. For comparison, Fig. 11 (in black) also plots the beacon derived fading over the same period, which for the rest of this article is assumed to be the reference fading value. It should be noted that the beacon and noise power measurements were averaged at 1 min intervals prior to the derived attenuations. The basis of averaging the measurements was to improve the resolution of the radiometer and the accuracy of the beacon power measurements. Also, the mean radiating temperature T_m was calculated as previously described. Consequently, the error of the radiometric measurement is next quantified by the difference from the beacon derived measurement. A first visual inspection indicates an overall good agreement between the two curves at least for low fading values. In order to further quantify this observation, Fig. 12 shows the difference (in dB) between the two sets of measurements. The mean value of this curve is 0.18 dB with a standard deviation of 0.13 dB. Moreover, the cumulative distribution function (CDF) curve of this data shows values less than 1 dB, 97.0% of the time. This indicates that the

probability to obtain a radiometric measurement of the fading with error less than 1 dB is 0.97. A similar analysis indicates that the radiometric measurement can offer better accuracy than 0.5 dB with a probability of 0.937.

Since it is theoretically expected that the radiometric measurements would be more accurate for the low fading regime, the accuracy of the radiometric estimations is next quantified when measurements over a certain fading threshold are excluded. In particular, thresholds of fading at 10, 5, 4, 3, and 2 dB are considered. The difference (in dB) between the two sets of measurements for a threshold is obtained and any values exceeding the set threshold are not considered. Fig. 12 (in magenta) shows the difference (in dB) between the radiometric and beacon derived attenuations for a threshold value of 3 dB.

It is noted that in practice, the low fading regime is of particular interest for the operation of satellite feeder links in the *Q*-/*V*-band and beyond. This is due to the limited offerings in power amplification technologies at these frequencies [31], which are likely to limit the fade margins of the gateway links compared with lower frequency bands. Indeed, in place of large fade margins, *Q*-/*V*-band feeder links increasingly rely on site diversity [32] as means to combat fading.

Consequently, a similar analysis is performed for the different threshold values. The CDF for the difference between the two sets of measurements when different threshold values are considered is plotted in Fig. 13. Table II provides some summary results indicating the probability as a percentage

TABLE II
CDF OF ≤0.5 AND ≤1 dB FOR ALL POINTS
AND DIFFERENT FADING THRESHOLDS

Fading Thresholds	CDF	
	≤ 0.5dB	≤ 1dB
None	93.7%	97.0%
≤ 10dB	94.2%	97.6%
≤ 5dB	96.1%	99.1%
≤ 4dB	97.2%	99.6%
≤ 3dB	98.5%	99.9%
≤ 2dB	99.0%	100.0%

for the radiometric measurement to deliver valid result within error margins of 0.5 and 1 dB for different fading estimation ranges. As shown, when targeting to obtain fading readings up to 5 dB, the probability of the error to be below 1 dB is 0.991. This probability reduces to 0.976 when fading up to 10 dB is targeted. It is noted that although in this article, the beacon derived fading is considered as reference, in practice there is some uncertainty also with this approach. This is indicated by, e.g., the standard deviation of the beacon derived fading over typical bright sky conditions being of the order of 0.25 dB. Moreover, calibration of any gain variation from the receiver would yield improved results and strengthen the accuracy for the use of a standalone radiometer for monitoring fading.

V. DISCUSSION AND CONCLUSION

A Q-band SDR-based terminal installed at Heriot-Watt University receiving the Aldo Paraboni beacon was used to evaluate the potential of utilizing digital noise power integration as an estimate for passive radiometry. Radiometric measurements of the atmosphere were derived from the calibrated integrated noise, and the results were compared against concurrent beacon derived measurements. The beacon and radiometric derived measurements indicated a good agreement, particularly in the low fading regime. Indicatively, and assuming the beacon derived measurement as a reference, the error probability of the SDR radiometer delivering error >1 dB for fadings up to 5 dB is of the order of 1%. This range and resolution can be suitable for the design of future Q-/V-band gateways and beyond, which due to technology constraints, are likely to operate at lower fade margins compared with the existing systems up to the Ka-band. However, in principle, the proposed setup and calibration methodology can achieve improved resolution based on hardware with superior performance and, in this case, can be exploited during the operation of a high-frequency link. According to prevailing standards [33], propagation impairment mitigation techniques (PIMTs), such as adaptive coding and modulation, will be deployed with a very fine granularity for the fading. Indicatively, we note that the entire spectrum of available coding rates for 16APSK modulation extends over the signal-to-noise ratio of about 6 dB [33]. Consequently, these findings reflect to potentially significant gains in the application of PIMT during deployment

while dispensing the need for additional costly instrumentation (e.g., dedicated radiometer) by virtue of enabling a built-in radiometric observation within the existing receiver hardware.

REFERENCES

[1] H. Fenech, A. Tomatis, S. Amos, J. S. Merino, and V. Soumpholphakdy, "An operator's perspective on propagation," in *Proc. 8th Eur. Conf. Antennas Propag. (EuCAP)*, Apr. 2014, pp. 3349–3352.

[2] A. Costouri *et al.*, "European w-band propagation campaign development," in *Proc. IEEE 12th Eur. Conf. Antennas Propag. (EuCAP)*, Apr. 2018, pp. 1–5.

[3] M. Aloisio, P. Angeletti, F. Coromina, and R. De Gaudenzi, "Exploitation of Q/V-band for future broadband telecommunication satellites," in *Proc. IVEC*, Apr. 2012, pp. 351–352.

[4] B. R. Arbesser-Rastburg and A. Paraboni, "European research on Ka-band slant path propagation," *Proc. IEEE*, vol. 85, no. 6, pp. 843–852, Jun. 1997.

[5] S. Ventouras, S. A. Callaghan, and C. L. Wrench, "Long-term statistics of tropospheric attenuation from the Ka/U band Italsat satellite experiment in the United Kingdom," *Radio Sci.*, vol. 41, no. 2, pp. 1–19, 2006.

[6] A. Paraboni, A. Vernucci, L. Zuliani, E. Colzi, and A. Martellucci, "New satellite experiment in the Q/V band for the verification of fade countermeasures based on the spatial non-uniformity of attenuation," in *Proc. 2nd Eur. Conf. Antennas Propag. (EuCAP)*, Jun. 2007, p. 555.

[7] S. Ventouras *et al.*, "Large scale assessment of Ka/Q band atmospheric channel across europe with ALPHASAT TDP5: The augmented network," in *Proc. 11th Eur. Conf. Antennas Propag. (EUCAP)*, Mar. 2017, pp. 1471–1475.

[8] *Cubesat-Based W-Band Channel Measurements*, ESA ARTES 5.1 Statement Work, Eur. Space Res. Technol. Centre, Noordwijk, The Netherlands, 2016.

[9] *Characterization of w-Band Propagation Channel Through Ground-Based Observations*, ESA ITT AO/1-9202/18/NL/AF, Statement Work, Eur. Space Res. Technol. Centre, Noordwijk, The Netherlands, 2018.

[10] J. E. Allnutt, *Satellite-to-Ground Radiowave Propagation*, 2nd ed. Edison, NJ, USA: IET, 2011.

[11] J. Nessel, J. Morse, M. Zemba, C. Riva, and L. Luini, "Performance of the NASA beacon receiver for the alphasat aldo paraboni TDP5 propagation experiment," in *Proc. IEEE Aerosp. Conf.*, Mar. 2015, pp. 1–8.

[12] C. J. Kikkert, B. J. Bowthorpe, and J. T. Ong, "Improvements to a DSP based satellite beacon receiver and radiometer," in *Proc. 2nd Int. Conf. Inf., Commun. Signal Process. (ICICS)*, 1999, pp. 7–10.

[13] J. Nessel, G. Gousetis, M. Zemba, and J. Houts, "Design and preliminary results from edinburgh, UK Alphasat Q-band propagation terminal," in *Proc. 22nd Ka Broadband Commun. Conf.*, Cleveland, OH, USA, 2016, pp. 1–11.

[14] A. Z. Papafragkakis, A. D. Panagopoulos, and S. Ventouras, "Combined beacon and noise satellite propagation measurements using software defined radio," in *Proc. 11th Eur. Conf. Antennas Propag. (EUCAP)*, Mar. 2017, pp. 2356–2360.

[15] A. Rocha, S. Mota, and F. Jorge, "Propagation campaign at Q-band and Ka-band using the alphasat and Ka-sat satellites," in *Proc. 12th Eur. Conf. Antennas Propag. (EuCAP)*, 2018, p. 904.

[16] *Propagation Data and Prediction Methods Required for the Design of Earth-Space Telecommunication Systems*, document ITU-R P.618-13, 2017.

[17] F. T. Ulaby *et al.*, *Microwave Radar and Radiometric Remote Sensing*, vol. 4, no. 5. Ann Arbor, MI, USA: Univ. Michigan Press, 2014.

[18] D. M. Pozar, *Microwave Engineering*. Hoboken, NJ, USA: Wiley, 2009.

[19] C. Mätzler, "Ground-based observations of atmospheric radiation at 5, 10, 21, 35, and 94 GHz," *Radio Sci.*, vol. 27, no. 3, pp. 403–415, May 1992.

[20] Y. Han and E. R. Westwater, "Analysis and improvement of tipping calibration for ground-based microwave radiometers," *IEEE Trans. Geosci. Remote Sens.*, vol. 38, no. 3, pp. 1260–1276, May 2000.

[21] M. J. Zemba, J. R. Morse, and J. A. Nessel, "Frequency estimator performance for a software-based beacon receiver," in *Proc. IEEE Antennas Propag. Soc. Int. Symp. (APSURSI)*, Jul. 2014, pp. 1574–1575.

[22] B. G. Quinn and J. M. Fernandes, "A fast efficient technique for the estimation of frequency," *Biometrika*, vol. 78, no. 3, pp. 489–497, 1991.

[23] H. J. Liebe, G. A. Hufford, and M. G. Cotton, "Propagation modeling of moist air and suspended water/ice particles at frequencies below 1000 GHz," in *Proc. Atmos. Propag. Effects Through Natural Man-Made Obscurants Visible MM-Wave Radiat. (AGARD)*, 1993, pp. 1–11.

[24] P. W. Rosenkranz, "Water vapor microwave continuum absorption: A comparison of measurements and models," *Radio Sci.*, vol. 33, no. 4, pp. 919–928, Jul. 1998.

[25] J. Nessel, M. Zemba, J. Morse, L. Luini, and C. Riva, "Preliminary statistics from the NASA alphasat beacon receiver in Milan, Italy," in *Proc. 9th Eur. Conf. Antennas Propag. (EuCAP)*, 2015, pp. 1–5.

[26] M. Zemba, J. Nessel, C. Riva, L. Luini, and G. Goussetis, "NASA's alphasat propagation terminals: Milan, italy, and edinburgh, scotland," *Int. J. Satell. Commun. Netw.*, vol. 37, no. 5, pp. 502–512, Sep. 2019.

[27] TK Instruments. *Absorber, Space Qualified Tessellating TeraHertz RAMs*. Accessed: 2008. [Online]. Available: http://www.terahertz.co.uk/tk-instruments/products/tesselatingterahertzram

[28] C. J. Kikkert and O. P. Kenny, "A digital signal processing based Ka band satellite beacon receiver/ radiometer," in *Proc. 2nd Int. Conf. Signal Process. Commun. Syst.*, Dec. 2008, pp. 1–8.

[29] J. M. Riera, A. Benarroch, P. García-del-Pino, and J. M. García-Rubia, "Simultaneous beacon and radiometer propagation measurements in the Ka-band," in *Proc. 5th Eur. Conf. Antennas Propag. (EuCAP)*, 2011, pp. 3958–3962.

[30] G. Brost, K. Magde, and W. Cook, "Radiometer based measurements of slant-path attenuation in the V/W bands," in *Proc. 13th Spec. Meeting Microw. Radiometry Remote Sens. Environ. (MicroRad)*, Mar. 2014, pp. 118–123.

[31] J. Moron et al., "A novel high-performance V-band GaN MMIC HPA for the QV-lift project," in *Proc. 24th Ka-Band Conf.*, Niagara Falls, ON, Canada, Oct. 2018, pp. 1–6.

[32] F. Massaro et al., "QV-LIFT project: Using the Q/V band Aldo Paraboni demonstration payload for validating future satellite systems," in *Proc. 23rd Ka BroadBand Commun., Navigat. Earth Observ. Conf.*, 2017, pp. 1–16.

[33] *Digital Video Broadcasting (DVB); Second Generation Framing Structure, Channel Coding and Modulation Systems for Broadcasting, Interactive Services, News Gathering and Other Broadband Satellite Applications*, Standard ETSI EN 302 307-2, 2014, pp. 1–139. [Online]. Available: https://www.etsi.org/deliver/etsi_en/302300_302399/30230702/01.01.01_20/en_30230702v010101a.pdf

Alexios Costouri was born in Nicosia, Cyprus. He received the B.Eng. degree (Hons.) in electrical and electronic engineering from Heriot-Watt University, Edinburgh, U.K., in 2016, where he is currently pursuing the Ph.D. degree in satellite communications and atmospheric propagation with the Institute of Signals, Sensors and Systems (ISSS).

During his time in the ISSS Microwave Group, he was responsible for the smooth operation of the mm-wave receivers for propagation measurements. Furthermore, he is responsible for the design, development, and implementation of the Ka-band receiver for propagation measurements. He has also contributed toward the development and design of a GEO W-band payload for European propagation measurements under an ESA TRP. His current research interests include digital radiometry, development of RF testbeds with the aid of software-defined radio (SDR) and USRPs, atmospheric propagation at mm-wave, and RF system design.

James Nessel (Member, IEEE) received the B.S. and M.S. degrees in electrical engineering from Arizona State University (ASU), Tempe, AZ, USA, in 2002 and 2004, respectively, and the Ph.D. degree from The University of Akron, Akron, OH, USA, in 2014, with a focus on active phase compensation of widely distributed antenna arrays.

He was with Los Alamos National Laboratories, ASU, where he was specialized in semiconductor device theory and involved in the development of models for predicting the effects of gamma radiation on semiconductor microelectromechanical systems devices with. Since 2004, he has been an Electronics Engineer with the Advanced High Frequency Branch, National Aeronautics and Space Administration (NASA) Glenn Research Center, Cleveland, OH. He is currently a Co-Investigator of the NASA's Atmospheric Propagation Studies Project. His current research interests include Ka-band propagation, microwave remote sensing, and active phase correction for transmit arraying of microwave signals.

George Goussetis (Senior Member, IEEE) received the Diploma degree in electrical and computer engineering from the National Technical University of Athens, Athens, Greece, in 1998, the Ph.D. degree from the University of Westminster, London, U.K., in 2002, and the B.Sc. degree (Hons.) in physics from University College London (UCL), London, in 2002.

In 1998, he joined Space Engineering, Rome, Italy, as an RF Engineer, and in 1999, the Wireless Communications Research Group, University of Westminster, as a Research Assistant. From 2002 to 2006, he was a Senior Research Fellow with Loughborough University, Loughborough, U.K. He was a Lecturer (Assistant Professor) with Heriot-Watt University, Edinburgh, U.K. from 2006 to 2009 and a Reader (Associate Professor) with Queen's University Belfast, Belfast, U.K., from 2009 to 2013. In 2013, he joined Heriot-Watt University as a Reader and was promoted to Professor in 2014, where he currently directs the Institute of Sensors Signals and Systems. He has authored or coauthored over 500 peer-reviewed articles, five book chapters, and one book, and he holds four patents. His research interests are in the area of microwave and antenna components and subsystems.

Dr. Goussetis has held a Research Fellowship from the Onassis Foundation in 2001, a Research Fellowship from the U.K. Royal Academy of Engineering from 2006 to 2011, and European Marie-Curie experienced researcher fellowships from 2011to 2012 and again from 2014 to 2017. He was a co-recipient of the 2011 European Space Agency Young Engineer of the Year Prize, the 2011 EuCAP Best Student Paper Prize, the 2012 EuCAP Best Antenna Theory Paper Prize, and the 2016 Bell Labs Prize. He has served as an Associate Editor for the IEEE ANTENNAS AND WIRELESS PROPAGATION LETTERS.